Inorganic Chemistry Cite This: Inorg. Chem. 2020, 59, 226–234

pubs.acs.org/IC

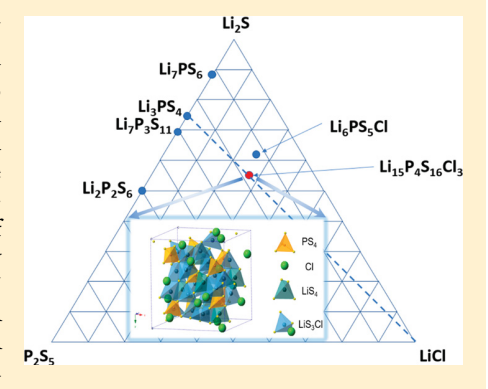
Li₁₅P₄S₁₆Cl₃, a Lithium Chlorothiophosphate as a Solid-State Ionic **Conductor**

Zhantao Liu, [†] Tatiana Zinkevich, [‡] Sylvio Indris, [‡] Xingfeng He, [§] Jue Liu, [⊥] Wenqian Xu, [∥] Jianming Bai, [¶] Shan Xiong, [†] Yifei Mo, [§] and Hailong Chen*, [†]

[†]The Woodruff School of Mechanical Engineering, Georgia Institute of Technology, Atlanta, Georgia 30332, United States [‡]Institute for Applied Materials, Karlsruhe Institute of Technology, Hermann-von-Helmholtz Platz 1, D-76344 Eggenstein-Leopoldshafen, Germany

Supporting Information

ABSTRACT: Tremendous efforts have been devoted to the design of solid Li⁺ electrolytes and the development of all-solid-state batteries. Compared with conventional Li-ion batteries, which use flammable liquid organic electrolytes, all-solid-state batteries show significant advantages in safety. In this work, a novel lithium chlorothiophosphate compound, Li₁₅P₄S₁₆Cl₃, is discovered. The crystal structure and electrochemical properties are investigated. Li₁₅P₄S₁₆Cl₃ can be synthesized as a pure phase via a facile solid-state reaction by heating a ballmilled mixture of Li₂S, P₂S₅, and LiCl at 360 °C. The crystal structure of Li₁₅P₄S₁₆Cl₃ was refined against neutron and synchrotron powder X-ray diffraction data, revealing that it crystallizes in the space group I43d. The Li⁺ transport in Li₁₅P₄S₁₆Cl₃ was also investigated by multiple solid-state NMR methods, including variable-temperature NMR line-shape analysis, NMR relaxometry, and pulsed-field-gradient NMR. Li₁₅P₄S₁₆Cl₃ shows good thermodynamic stability and can be synthesized at relatively low temperature.



Although it exhibits a low ionic conductivity at room temperature, it can serve as a new motif crystal structure for the design and development of new solid-state electrolytes.

■ INTRODUCTION

All-solid-state Li-ion batteries (ALSOLIBs) are considered to be an emerging battery technology for next-generation electrochemical energy storage. Currently used commercial Li-ion batteries (LIBs) contain flammable organic electrolytes, which may cause fire or explosion in harsh or abusive environments. Compared with commercial LIBs, ALSOLIBs with nonflammable solid electrolytes (SEs) not only have much better safety properties but also potentially have higher energy density if a Li-metal anode can be enabled.1-

As the key component of an ALSOLIB, the SE must meet the requirements in multiple categories of properties, including high ionic conductivity at ambient temperature, good chemical and electrochemical stability, good mechanical durability, etc. Commonly, SEs with room temperature (RT) ionic conductivity higher than 10⁻⁴ S cm⁻¹ are preferred. 5,6 To date, predominantly two groups of SEs have attracted much attention: sulfide-based and oxide-based electrolytes. Oxide electrolytes, such as compounds with perovskite, NASICON, or garnet structures, exhibit RT ionic conductivity from 10⁻⁵ to

10⁻³ S cm^{-1,7-9} However, large grain-boundary (GB) resistance was often observed because of the poor electrical contact among the particles. High-temperature sintering may help to mitigate the GB resistance, which significantly increases the complexity and cost of the manufacturing process 10-12 and may result in unwanted side reactions with the cathode materials. 13,14 In contrast, sulfide SEs are soft and ductile. Good electrical contact among the particles and thus low GB resistance can be relatively easily achieved by facile cold pressing. 15 A number of lithium sulfides with high RT ionic conductivities, reaching or even exceeding 10⁻³ S cm⁻¹, have been reported, ^{16–18} including Li₃PS₄–Li₄GeS₄ solid solutions with LISICON structure, ¹⁹ Li₆PS₅X (X = Cl, Br, I) with argyrodite structure, ^{20–23} Li₇P₃S₁₁ glass ceramics, ²⁴ Li₁₀GeP₂S₁₂ (LGPS), ²⁵ etc. Some of these SEs, such as LGPS exhibit years high PT ionic conductivities of 10⁻² S cm⁻¹ LGPS, exhibit very high RT ionic conductivity of 10^{-2} S cm⁻¹, which exceeds that of liquid electrolytes, ²⁶ demonstrating the

Received: June 12, 2019 Published: December 12, 2019



[§]Department of Materials Science and Engineering, University of Maryland, College Park, Maryland 20742, United States

 $^{^{\}perp}$ Neutron Scattering Division, Oak Ridge National Laboratory (ORNL), Oak Ridge, Tennessee 37831, United States

X-ray Science Division, Advanced Photon Source (APS), Argonne National Laboratory (ANL), Argonne, Illinois 60439, United

[¶]National Synchrotron Light Source II, Brookhaven National Laboratory, Upton, New York 11973, United States

great potential of sulfide SEs. However, most of these known sulfide SEs require sophisticated processing (such as long-time, high-speed ball milling and precise control of the starting materials) and high-temperature (>500 °C) synthesis to achieve the expected high conductivities. 17 SEs with not only high RT conductivity but also facile and low-cost synthesis are still very much desired. From the crystal structure point of view, all of these known sulfide SEs only present a few limited types of crystal structures. Most of the current designs and developments of SEs are focused on elementary modifications based on these known structure types, which can be limited sometimes. The addition of new crystal structure motifs is also desired. Compared with the relatively extensively explored Li-P-S ternary phase diagram, the quaternary phase diagrams of Li-P-S-X (X = halogen elements) are much less explored, which provides high potential to find new prototypes of Li-ionconducting crystal structures. For example, Li₄PS₄I was recently reported and its ionic conductivity is 1.2×10^{-4} S cm⁻⁶. One group of Li-P-S-X compounds, the argyrodites Li_6PS_5X (X = Cl, Br, I), recently attracted a lot of attention because of their high conductivities, 5,21,27,28 demonstrating the high potential of these quaternary compounds. Besides the argyrodites, no other Li-P-S-X quaternary compounds have been reported, and a large area in the phase diagram remains unexplored. Recent computational works predicted that Li₁₅P₄S₁₆Cl₃^{29,30} can be thermodynamically stable. However, no synthesis conditions and crystal structure information were disclosed to date. Here we successfully synthesized a new compound, Li₁₅P₄S₁₆Cl₃, with a new crystal structure distinguished from all known sulfide SEs. The structural characterizations and ionic conduction behaviors of the compound are elaborated below.

METHODS

Materials Synthesis. Li $_1{\rm S}P_4S_{16}{\rm Cl}_3$ was synthesized via a ball-milling and subsequent calcination process. The starting materials Li $_2{\rm S}$ (99.98%, Sigma-Aldrich), $P_2{\rm S}_5$ (99%, Sigma-Aldrich), and LiCl (>99%, Sigma-Aldrich) were weighed in the desired molar ratio and mixed in a high-energy planetary ball mill (PM 200, Retsch) using a zirconia jar. A total of 10 zirconia balls of 10 mm diameter were put into each jar. The starting materials were ball-milled for 20 h at a rotation speed of 370 rpm. The ball-milled mixture was then pressed into pellets of $^1/_2$ -in. diameter and sealed in a quartz tube. The pellets were heated at 360 °C for 20 h and cooled inside the furnace. The pellets were ground into powder in an agate mortar and kept in an Argas-filled glovebox for the following characterizations. All materials were handled under an Ar atmosphere during the synthesis, characterization, and electrochemical testing processes.

Characterizations. X-ray diffraction (XRD) data of the powder samples were first collected by using a D8 Advance X-ray diffractometer (Bruker AXS) with Mo radiation ($\lambda_{K\alpha_1} = 0.7093$ Å). In situ XRD data of the synthesis process were also collected using a heat chamber (HTK1200N, Anton Paar) mounted on the diffractometer as follows. The powder of a ball-milled mixture of starting materials was filled in a quartz capillary in a glovebox and sealed. The tube was used for in situ XRD data collection and heated from RT to 440 °C. XRD data were collected in a step size of 20 °C, while the temperature was kept constant during each XRD scan.

Synchrotron XRD and pair-distribution-function (PDF) data were collected at beamline 17-BM-B at the APS at ANL, with a wavelength of 0.24116 Å. High-quality powder neutron diffraction (ND) data were collected on beamline POWGEN at the Spallation Neutron Source (SNS) at ORNL using the frame with a center wavelength of 0.8 Å. Rietveld refinement against the XRD and ND data was performed using *GSAS-II* and *TOPAS* (version 6) software. ^{31,32} The conversion from time-of-flight (TOF) to *d* spacing was done using a

second-order polynomial function (TOF = d0 + dfc*d + dfa*d²) calibrated from a NIST Si 640e standard sample. During the refinement, d0 and dfc were fixed to the values refined from the Si standard, while dfa was allowed to vary to account for the sample displacement. The crystal structure model obtained from the Rietveld refinement was used as the starting model for analysis of the PDF data. The X-ray PDF data were processed using PDFgetX3. 33 The total scattering structure factor S(Q) data were Fourier-transformed to the PDF with a maximum Q range $(Q_{\rm max})$ of 19 Å $^{-1}$. The collected data were corrected for background and sample absorption. PDFgui and TOPAS (version 6) were used for PDF data analysis. 32,34

Scanning electron microscopy (SEM) images were taken by using a Hitachi SU8010 scanning electron microscope. The sample was transferred from the glovebox in a well-sealed container to minimize air exposure.

 6 Li and 31 P magic-angle-spinning (MAS) NMR spectroscopy was performed with a Bruker Avance 500 MHz spectrometer. The magnetic field of 11.7 T corresponds to Larmor frequencies of 73.6 MHz for 6 Li and 202.5 MHz for 31 P. The samples were rotated in 2.5 mm zirconia rotors at a spinning speed of 20 kHz. All spectra were acquired with a Hahn-echo pulse sequence. 35 The chemical shifts were referenced to an aqueous 1 M 6 LiCl solution for 6 Li NMR and to $\rm H_3PO_4$ (85%) for 31 P NMR.

Temperature-dependent measurements of static $^7\mathrm{Li}$ NMR line shapes and $^7\mathrm{Li}$ spin—lattice relaxation times were performed with a Bruker 200 MHz spectrometer at a magnetic field of 4.7 T, on samples sealed in 10 mm glass vials. These spectra were acquired with a quadrupolar-echo sequence, a $\pi/2$ pulse length of about 3 $\mu\mathrm{s}$, and a recycle delay of 20 s. $^7\mathrm{Li}$ T_1 measurements were performed with a saturation—recovery pulse sequence. 36,37 $^7\mathrm{Li}$ pulsed-field-gradient (PFG) NMR measurements were acquired with a stimulated-echo sequence including bipolar gradients, on a Bruker Avance 300 MHz spectrometer operated with a Diff50 probe that provides pulsed-field gradients up to 30 T m $^{-1.38}$

Ab Initio Molecular Dynamics (AIMD) Simulations. Density functional theory (DFT) calculations were conducted using the Vienna ab initio simulation package $(VASP)^{39}$ within the projector-augmented-wave approach with a Perdew–Burke–Ernzerhof⁴⁰ generalized gradient approximation. AIMD simulations were performed to investigate Li diffusion. Γ -centered k points in the non-spin-polarized DFT calculations were used. The time step was 2 fs. The NVT ensemble using a Nosé–Hoover thermostat⁴¹ was used. The total time of the AIMD simulations was in the range of 100-600 ps. The ionic conductivity and error bars were calculated and estimated following previously established methods. 42

Electrochemical Measurements. The ionic conductivity was determined by an electrochemical impedance spectroscopy (EIS) method with an electrochemical impedance analyzer (VMP3, Bio-Logic) and a custom-built electrochemical cell. Typically, $\sim\!130$ mg of $\rm Li_{15}P_4S_{16}Cl_3$ powder was pressed into a pellet with a diameter of $^1/_2$ in. at a pressure of 100 bar. Two stainless steel rods were used as the current collectors. EIS data were collected in the temperature range of 30–90 °C at frequencies between 1 MHz and 1 Hz and with alternating-current amplitude of 500 mV.

■ RESULTS AND DISCUSSION

The quaternary Li-P-S-Cl phase diagram can be plotted in an equivalent Li₂S-P₂S₅-LiCl ternary phase diagram with better clarity, as shown in Figure 1. The argyrodite Li₆PS₅Cl is the only known phase in the middle of the phase diagram, but it is very unlikely that it is the only phase. In this phase diagram, Li₂S, LiCl, P₂S₅, and Li₃PS₄ are considered thermodynamically stable, while Li₇P₃S₁₁, day are considered thermodynamically stable, while Li₇P₃S₁₁, Li₇PS₆, and Li₆PS₅Cl⁴⁵ were predicted to be metastable in static DFT calculations at 0 K. Previous studies showed that the formation energy of Li₁₅P₄S₁₆Cl₃ is 8 meV atom⁻¹, indicating that Li₁₅P₄S₁₆Cl₃ is just slightly metastable in the relevant Li-P-S-Cl phase diagram, similar to Li₇P₃S₁₁, Li₇PS₆, and

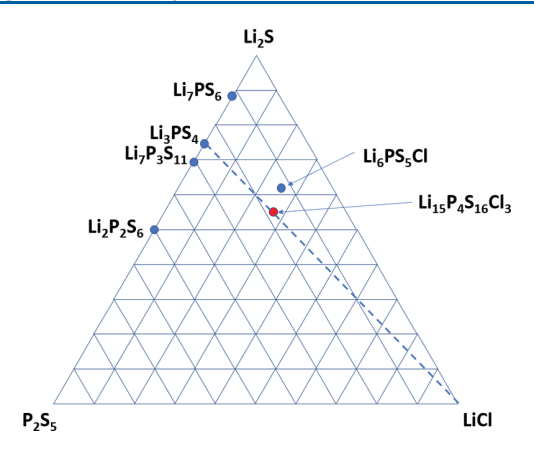


Figure 1. Li–P–S–Cl quaternary phase diagram plotted in a Li₂S– P_2S_5 –LiCl ternary manner.

 $\text{Li}_6\text{PS}_5\text{Cl.}^{4.5}$ The formation energy of $\text{Li}_{15}\text{P}_4\text{S}_{16}\text{Cl}_3$ from the precursor phases Li_2S , P_2S_5 , and LiCl is -3.203 eV atom⁻¹, indicating that it is an energetically favorable formation during the synthesis. Therefore, we conducted a systematic exploration on select regions of the phase diagram with the help of in situ XRD for the synthesis. The Li-rich region on the top right area of the phase diagram was first explored, and one new phase was quickly identified. In situ XRD was performed on the solid-state synthesis of the starting materials with various material ratios. Figure 2 shows the in situ XRD patterns

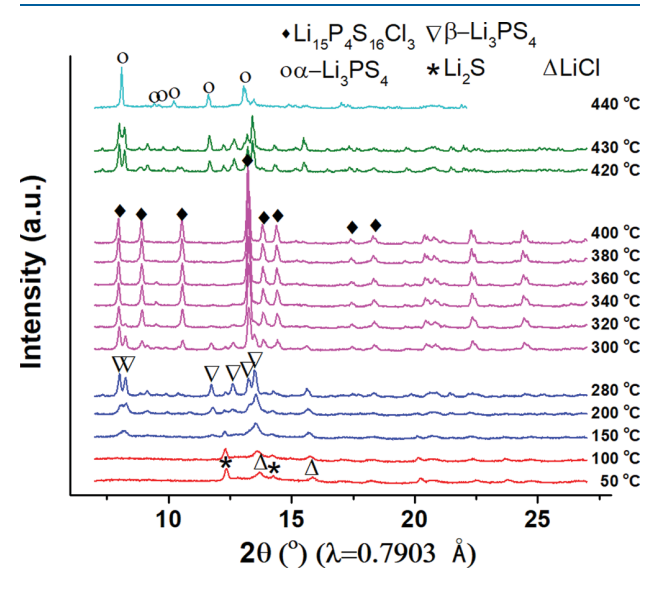


Figure 2. In situ XRD patterns of ball-milled starting materials Li_2S , P_2S_5 , and LiCl with a molar ratio of 3:1:1.5, heated from 50 to 440 $^{\circ}\text{C}$.

collected from the starting materials with a ratio of $\text{Li}_2\text{S:P}_2S_5$:LiCl = 3:1:1.5. The sample was heated from RT to 450 °C. The diffraction pattern at 50 °C shows the amorphous characteristics of the ball-milled mixture and diffraction peaks with relatively low intensity, which can be indexed using the minor phases Li_2S and LiCl. As the temperature increases, the intensities of these peaks increase, indicating increasing crystallinity of Li_2S and LiCl. Once the temperature reaches 150 °C, the reflections associated with the Li_2S phase start to diminish, which is accompanied by the appearance of

reflections belonging to the $\beta\text{-Li}_3\text{PS}_4$ phase. At 300 °C, a new set of reflections emerge that cannot be indexed to a commonly known lithium thiophosphate compound. Meanwhile, the intensities of the reflections associated with the $\beta\text{-Li}_3\text{PS}_4$ and LiCl phases start to decrease, implying that a new phase forms from the reaction between $\beta\text{-Li}_3\text{PS}_4$ and LiCl. The mixture is fully converted into the new phase at 340 °C, where no more reflections from $\beta\text{-Li}_3\text{PS}_4$ and LiCl can be seen. The new phase is stable up to 400 °C and decomposes to $\beta\text{-Li}_3\text{PS}_4$ and LiCl at 420 °C. $\beta\text{-Li}_3\text{PS}_4$ turns into $\alpha\text{-Li}_3\text{PS}_4$ above 440 °C.

Because no other phases were seen at $360\,^{\circ}\text{C}$, it can be assumed that all starting materials were converted to this new phase. Therefore, the ratio of the elements in this new phase is Li:P: S: Cl = 15:4:16:3, and the formation reaction can be written as follows:

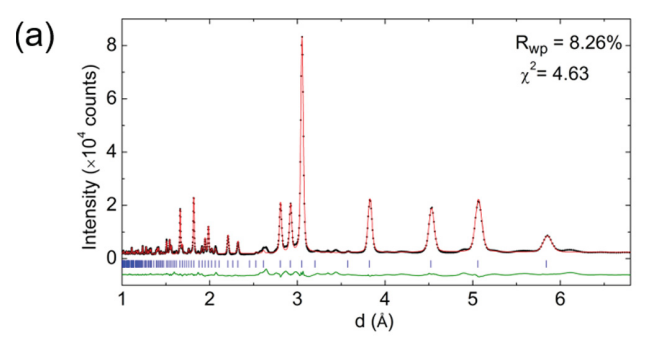
$$4\text{Li}_{3}\text{PS}_{4} + 3\text{LiCl} \rightarrow \text{Li}_{15}\text{P}_{4}\text{S}_{16}\text{Cl}_{3}$$
 (1)

Li₁₅P₄S₁₆Cl₃ is a new composition, whose detailed crystal structure has not been reported. However, its Ag analogue, Ag₁₅P₄S₁₆Cl₃, does exist, and its XRD pattern very much resembles the pattern observed in Figure 2. Given the similarity in the charges and ionic radii of Ag+ and Li+, the similar XRD patterns strongly imply that the actual elementary composition of the new phase is likely Li₁₅P₄S₁₆Cl₃. To verify this assumption, high-resolution powder synchrotron XRD data were collected and Rietveld refinement of the structure was performed using the space group of Ag₁₅P₄S₁₆Cl₃ as the starting model, but with all Ag atoms replaced by Li atoms. Figure 3 shows the refinement result using the $\overline{143}d$ space group. A high-quality fitting with a $R_{\rm wp}$ value of 8.26% was achieved, confirming that this new compound indeed has a structure similar to that of Ag₁₅P₄S₁₆Cl₃. This has been further confirmed by the good-quality refinement of the intermediaterange structure using X-ray PDF (R_w=18.6%). The minor discrepancy in the low r range may result from a small amount of the amorphous phase, as reported before. 46,47

The Li positions were further confirmed using Fourier difference map analysis of both powder ND and synchrotron XRD data, as shown in Figure S1. It clearly indicates the two plausible Li sites, which match well with those Li positions obtained from Rietveld refinements.

The final Rietveld refinement of the crystal structure of $\operatorname{Li}_{15} P_4 S_{16} Cl_3$ against the ND data is shown in Figure 4. The refined cell parameter a of 14.3052(3) Å is smaller to that of $\operatorname{Ag}_{15} P_4 S_{16} \operatorname{Cl}_3$ (a=14.838 Å), 48 in accordance with the fact that Li^+ has a smaller ionic radius (0.59 Å, four-coordinated) relative to Ag^+ (1.00 Å, four-coordinated). The crystallographic information extracted from the ND data is listed in Table 1. The crystal structure drawn based on the refinement result is shown in Figure 5. The structure is built by three kinds of tetrahedra: PS_4 , LiS_4 , and $\operatorname{Li}(S_3\operatorname{Cl})$. All tetrahedra are connected via common corners. Every S or Cl atom is cornershared by four tetrahedra. Li atoms occupy two different tetrahedral sites: $\operatorname{Li}(1)$ occupies the 12a site and is bonded to four S^{2-} ions, while $\operatorname{Li}(2)$ occupies the 48e site and is bonded to three S^{2-} ions and one Cl^- ion.

SEM images of as-synthesized $\text{Li}_{15}\text{P}_4\text{S}_{16}\text{Cl}_3$ are shown in Figure 6. The primary particles with dimensions ranging from 1 to 5 μ m are of cubic/cuboid shape, in accordance with their space group symmetry. The primary particles are agglomerated to form secondary particles of a few tens of micrometers, which



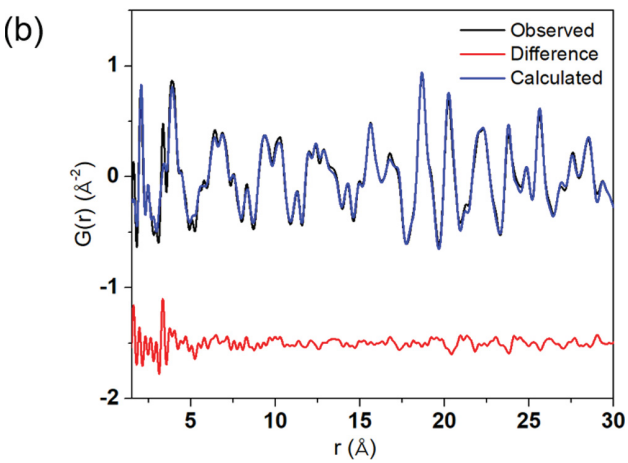


Figure 3. (a) Rietveld refinement of the long-range structure of $\text{Li}_{15}\text{P}_4\text{S}_{16}\text{Cl}_3$ against synchrotron XRD data ($\lambda=0.24116$ Å). (b) Least-squares refinement of the intermediate-range structure of $\text{Li}_{15}\text{P}_4\text{S}_{16}\text{Cl}_3$ using synchrotron X-ray PDF data.

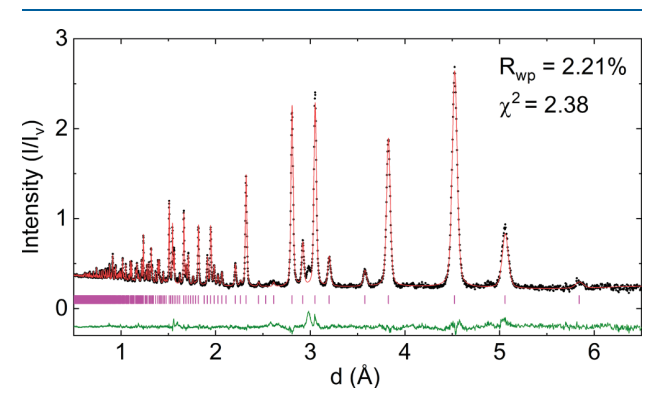


Figure 4. Rietveld refinement of $\text{Li}_{15}\text{P}_4\text{S}_{16}\text{Cl}_3$ against the TOF ND data (POWGEN). The black dots are the experiment data, the red curve is the calculated data, and the green curve is the difference. The Bragg reflections are shown as blue markers. There is one unidentified peak around 3 Å, indicating the coexistence of impurity phase(s).

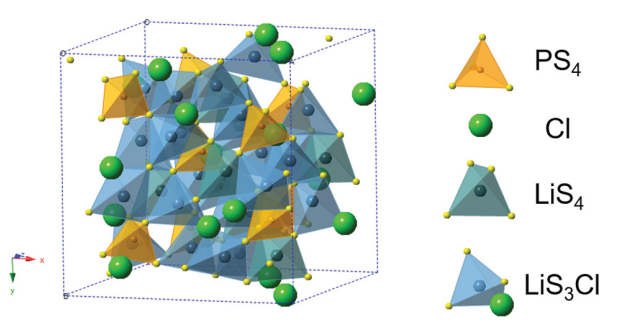


Figure 5. Refined crystal structure of $\text{Li}_{15}\text{P}_4S_{16}\text{Cl}_3$ using the powder ND data.

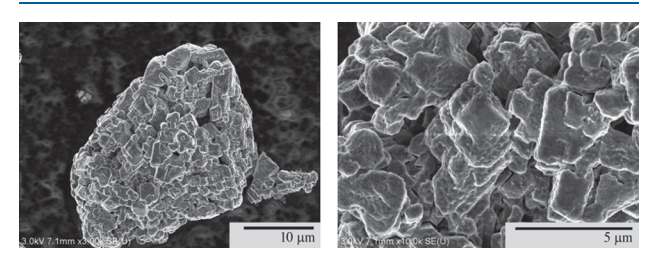


Figure 6. SEM images of Li₁₅P₄S₁₆Cl₃.

is likely due to the fact that the sample was cooled from a molten phase.

The local structures around the Li and P ions were investigated by 6Li and 31P MAS NMR spectroscopy, respectively. The spectra are shown in Figure 7. The ⁶Li NMR spectrum (Figure 7a) reveals two well-resolved narrow peaks. The stronger one at 1.0 ppm can be assigned to the Li(2) site at the 48e position, and the weaker peak is assigned to the Li(1) site at the 12a position. The ³¹P NMR spectrum (Figure 7b) shows two well-resolved peaks at 88.8 and 85.7 ppm. Both can be assigned to isolated [PS₄]³⁻ tetrahedra in the crystal structure, 46 in agreement with the crystal structure derived from XRD/ND. The fact that two very similar environments are visible in the ³¹P NMR spectrum even though only one site was determined by XRD/ND could hint at the existence of a small amount of the amorphous phase. We ascribe the peak at 88.8 ppm to [PS₄]³⁻ from crystalline Li₁₅P₄S₁₆Cl₃ and the peak at 85.7 ppm to the amorphous phase, based on the observation that the intensity of the peak at 85.7 ppm decreases as the heating time is extended and the crystallinity increases.

The conductivity of $\text{Li}_{15}\text{P}_4\text{S}_{16}\text{Cl}_3$ was measured by EIS. The relative density of the pellet is about 80%, under a uniaxial pressure of 10 MPa. Bulk and GB contributions to the total resistance cannot be deconvoluted (Figure S2). Figure 8 shows the temperature dependence of the conductivity of $\text{Li}_{15}\text{P}_4\text{S}_{16}\text{Cl}_3$. $\text{Li}_{15}\text{P}_4\text{S}_{16}\text{Cl}_3$ exhibited a low ionic conductivity

Table 1. Refined Structure of Li₁₅P₄S₁₆Cl₃ [Space Group $\overline{143}d$; a = 14.3052(3) Å] Using the ND Data

site	Wyckoff	\boldsymbol{x}	у	z	Occ.	$B_{\rm iso}({ m \AA}^2)$
Li(1)	12a	0.00000	0.25000	0.37500	1	1.85(7)
Li(2)	48e	0.1420(3)	0.2145(3)	0.5825(4)	1	1.85(7)
S(1)	16c	0.0320(2)	0.0320(2)	0.0320(2)	1	1.09(4)
S(2)	48e	0.1080(2)	0.3433(2)	0.4713(2)	1	1.09(4)
Cl(1)	12b	0.00000	0.25000	0.87500	1	1.71(4)
P(1)	16c	0.1997(1)	0.1997(1)	0.1997(1)	1	0.90(4)

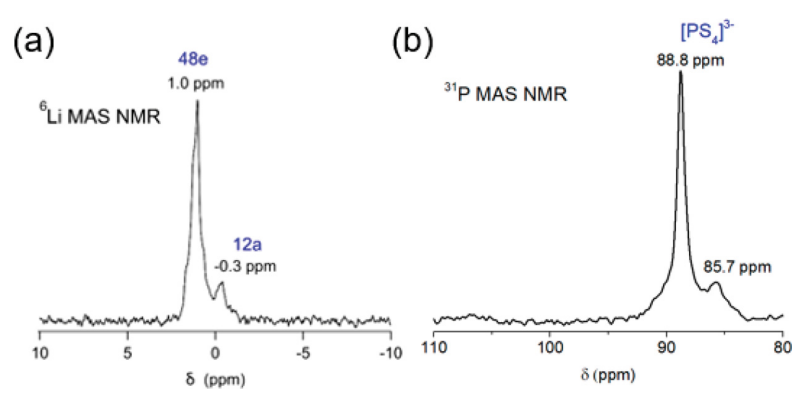


Figure 7. ⁶Li and ³¹P MAS NMR spectra of Li₁₅P₄S₁₆Cl₃.

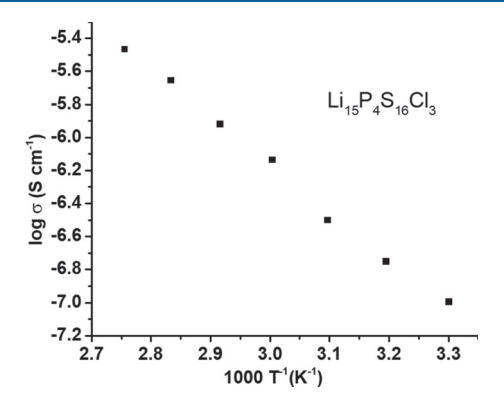


Figure 8. Arrhenius plot of ${\rm Li_{15}P_4S_{16}Cl_3}$. The activation energy is 0.57 eV.

of 1.0 \times 10⁻⁷ S cm⁻¹ at 30 °C, which is similar to those of β -Li₃PS₄ (9 \times 10⁻⁷ S cm⁻¹) and γ - Li₃PS₄ (3 \times 10⁻⁷ S cm⁻¹). When the temperature was increased to 90 °C, the ionic conductivity reached 3.4 \times 10⁻⁶ S cm⁻¹. The calculated activation energy is 0.57 eV, which is different from those of β -Li₃PS₄ (0.16 eV) and γ - Li₃PS₄ (0.22 eV). This value is also much higher than those of typical Li-ion conductors such as Li₇P₃S₁₁, Li₆PS₅Cl, and LGPS.

AIMD was also used to calculate the theoretical ionic conductivity of this compound. The calculated ionic conductivity is around 10⁻¹⁴ S cm⁻¹, which is much lower than the experimental results. The conductivity of the sample being much higher than the calculated theoretical value may be caused by the existence of a small amount of the amorphous impurity phase and defects in the Li₁₅P₄S₁₆Cl₃ material. The amorphous impurity phase may be more conductive than Li₁₅P₄S₁₆Cl₃, which increases the overall measured conductivity. The other reason is that formation of the impurity could result in a slight off-stoichiometry in Li₁₅P₄S₁₆Cl₃, and mobile defects, such as Li vacancies or interstitial Li ions, may exist in the Li₁₅P₄S₁₆Cl₃ material, which increases the conductivity. In the AIMD computation, a perfect bulk-phase crystal Li₁₅P₄S₁₆Cl₃ with no preexisting defects was used, which may result in a limited carrier concentration for ion conduction. These differences in the experiments and computation may have resulted in the differences in the conductivity values. The results of the theoretical calculation suggest that Li ions at both the Li(1) and Li(2) sites are involved in the diffusion pathway. The mean-squared displacement—time (MSD-t) relationship (Figure S3) and Li trajectories within 2 ps at 1150 K (Figure

9) indicated that the Li diffusion path in $\text{Li}_{15}\text{P}_4\text{S}_{16}\text{Cl}_3$ is three-dimensional.

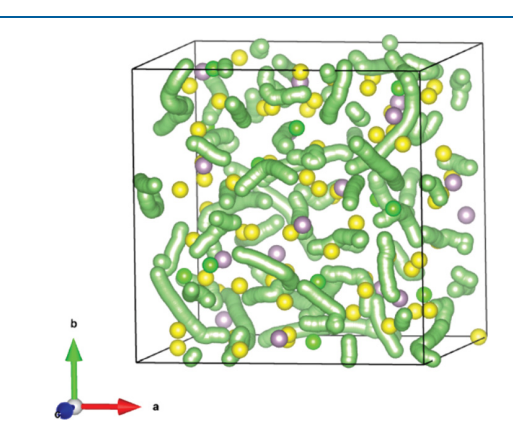


Figure 9. Li trajectories within 2 ps at 1150 K, as obtained from AIMD simulation.

In addition to its ability to investigate local structures element-specifically, solid-state NMR is also a powerful tool to probe the dynamics of mobile ions in solids on different time and length scales. Figure 10a shows the temperature dependence of static $^7\mathrm{Li}$ NMR spectra of $\mathrm{Li}_{15}P_4S_{16}\mathrm{Cl}_3$.

At low temperatures, the spectra consist of three different contributions, all centered around 0 ppm: (i) a broad contribution in the range from +25 to -25 ppm represents the satellite transitions of the ⁷Li nuclei (nuclear spin $I = \frac{3}{2}$), (ii) a narrower signal between +3 and −3 ppm represents the central transition, and (iii) a very narrow component with a width of about 0.5 ppm represents Li ions that are already mobile at these low temperatures. When the temperature is increased, the broader contributions show a clear so-called motional narrowing. This reflects the temporal averaging of the local environments around the Li ions due the increasingly fast motions of these ions. At 663 K, only a single contribution is visible in the static ⁷Li NMR spectrum. The width of the broader component is plotted versus temperature in Figure 10b. The curve shows no clear plateau at low temperatures and thus reveals that the motional averaging already started well below RT. The motion of the Li ions was additionally probed on very short time scales (few nanoseconds) by measuring the ⁷Li NMR relaxation rates T_1^{-1} as a function of the (inverse) temperature (Figure 10c). A clear maximum, as was observed for Li₃PS₄ or Li₁₀SnP₂S₁₂, could not be observed for

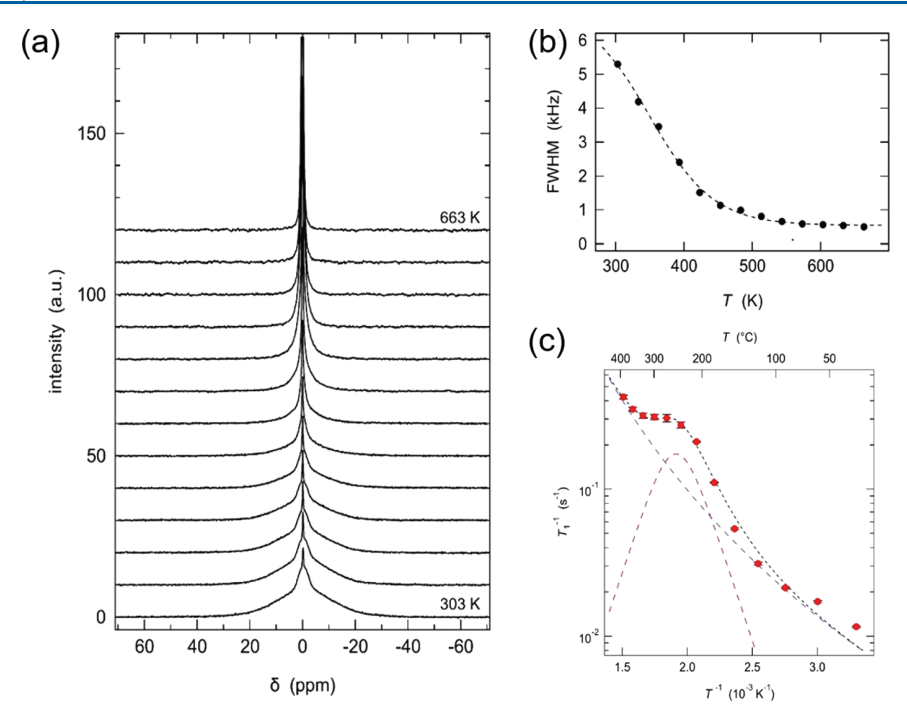


Figure 10. (a) Static 7 Li NMR spectra at temperatures between 303 and 663 K. (b) Full-width at half-maximum (FWHM) versus temperature for the broad component in the static 7 Li NMR spectra. (c) 7 Li NMR spin—lattice relaxation rates T_1^{-1} versus inverse temperature.

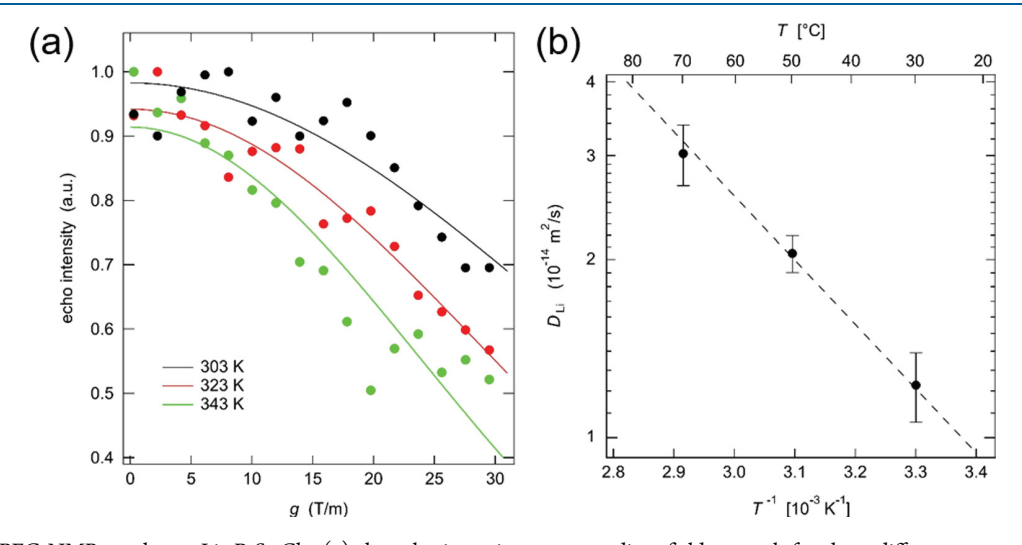


Figure 11. ⁷Li PFG NMR results on $\text{Li}_{15}P_4S_{16}\text{Cl}_3$: (a) the echo intensity versus gradient-field strength for three different temperatures (gradient duration $\delta=3$ ms; diffusion time $\Delta=300$ ms); (b) derived diffusion coefficients versus inverse temperature.

 ${\rm Li_{15}P_4S_{16}Cl_3}$. The relaxation rate rather shows a monotonic increase with increasing temperature and a shoulder at 523 K. The data can be described by a superposition of the diffusion-induced maximum^{37,51} and power law contribution (dashed lines in Figure 10c), which is an approach commonly used to describe such data. The latter one might represent another jump process with a maximum at temperatures too high to be reached in these experiments. The fact that a clear maximum in the overall data is not visible can be ascribed to the quite slow diffusion and thus to a smaller diffusion-induced contribution.

This behavior reveals a quite complex diffusion mechanism involving different jump processes between different Li sites. The diffusion-induced maximum reveals an average hopping rate of the Li ions of about $5\times10^8~{\rm s}^{-1}$ at 523 K and an

activation barrier for these jumps of 0.53 \pm 0.06 eV. From the jump rate, a Li ion conductivity of about 10^{-6} S cm⁻¹ can be extrapolated for 298 K. These values are in good agreement with the EIS results.

PFG NMR experiments were performed to study the long-range transport of Li ions, on the time scale of about 1 s. The echo damping is shown in Figure 11a for three different temperatures. As expected, a stronger echo damping is observed with increasing temperature due to faster Li diffusion. The echo damping as a function of the gradient-field strength g can be well described with a Gaussian function according to the Sejskal—Tanner equation 53 (solid lines in Figure 11a). The derived diffusion coefficients are displayed versus inverse temperature in Figure 11b. They show an Arrhenius-type

behavior with an activation energy of 0.22 \pm 0.04 eV. At 298 K, a diffusion coefficient of 10^{-14} m² s⁻¹ can be estimated. Assuming an uncorrelated, three-dimensional motion of all Li ions and using the number density of all Li ions $(2 \times 10^{28}$ m^{-3}), this would correspond to a Li ion conductivity of 1.3 \times 10⁻⁵ S cm⁻¹, as derived from the Nernst-Einstein equation. This value is higher than the total conductivity measured with EIS, and also the activation energy derived from PFG NMR is much lower than the 0.57 eV measured with EIS. This might hint at a stronger influence of the GBs on the impedance data than on the PFG results that are probing the transport on a time scale of 0.3 s and thus on a length scale of 0.1 μ m. Overall, the NMR results reveal a complex motion of the Li ions involving different types of jump processes, as expected from the crystal structure. The relatively slow dynamics of the Li ions is probably caused by the fully occupied Li(1) and Li(2) sites and the quite dense crystal structure. This provides multiple possibilities for future materials optimization, e.g., via cation and anion doping.

CONCLUSION

Li₁₅P₄S₁₆Cl₃, a new crystalline thiophosphate, was successfully synthesized for the first time. It is a novel quaternary compound in the Li-P-S-Cl system, in addition to the argyrodite Li₆PS₅Cl. The crystal structure of Li₁₅P₄S₁₆Cl₃ was identified and confirmed by synchrotron XRD and ND. Although the RT conductivity of this material is low, which may not have practical use in devices that require high ionic conductivities such as solid-state batteries, evidence in both computational predictions and our ongoing follow-up experiments has shown that the conductivity can be drastically improved by cation or anion doping/replacement in this crystal structure, which shows the value of the identification of a new compound as the motif structure for solid-state ionic conductors. The very low formation temperature (<350 °C) and good thermodynamic stability also imply that it can be a good basic structure for design. In fact, we have tried to synthesize $\text{Li}_{15}\text{P}_4\text{S}_{16}\text{Br}_3$ and $\text{Li}_{15}\text{P}_4\text{S}_{16}\text{I}_3$. $\text{Li}_{15}\text{P}_4\text{S}_{16}\text{Br}_3$ can also be successfully obtained at a lower temperature, implying abundant possibilities of future materials design, similar to what has been done with argyrodites, which may lead to new ionic conductors with higher conductivity or better stability.

ASSOCIATED CONTENT

S Supporting Information

The Supporting Information is available free of charge at https://pubs.acs.org/doi/10.1021/acs.inorgchem.9b01751.

Crystal structure and ${\rm Li^+}$ diffusion properties of ${\rm Li_{15}P_{4}S_{16}Cl_{3}}$ (PDF)

Accession Codes

CCDC 1935657 contains the supplementary crystallographic data for this paper. These data can be obtained free of charge via www.ccdc.cam.ac.uk/data_request/cif, or by emailing data_request@ccdc.cam.ac.uk, or by contacting The Cambridge Crystallographic Data Centre, 12 Union Road, Cambridge CB2 1EZ, UK; fax: +44 1223 336033.

AUTHOR INFORMATION

Corresponding Author

*Email: hailong.chen@me.gatech.edu (H.C.).

ORCID ®

Sylvio Indris: 0000-0002-5100-113X Jue Liu: 0000-0002-4453-910X Yifei Mo: 0000-0002-8162-4629 Hailong Chen: 0000-0001-8283-2860

Notes

The authors declare no competing financial interest.

ACKNOWLEDGMENTS

X.H. and Y.M. acknowledge support from the National Science Foundation under Award 1550423, the computational facilities from the University of Maryland supercomputing resources, the Maryland Advanced Research Computing Center, and the Extreme Science and Engineering Discovery Environment supported by the National Science Foundation under Award DMR150038. Z.L. and H.C. acknowledge financial support by the U.S. National Science Foundation under Grant CBET-1706723 and a new faculty startup fund of Georgia Institute of Technology. This research used resources of the Advanced Photon Source and National Synchrotron Light Source II, U.S. Department of Energy (DOE) Office of Science User Facilities operated for the DOE Office of Science by Argonne National Laboratory under Contract No. DE-AC02-06CH11357 and by Brookhaven National Laboratory under Contract No. DE-SC0012704.

REFERENCES

- (1) Auvergniot, J.; Cassel, A.; Ledeuil, J.-B.; Viallet, V.; Seznec, V.; Dedryvère, R. Interface Stability of Argyrodite $\text{Li}_6\text{PS}_5\text{Cl}$ toward LiCoO_2 , $\text{LiNi}_{1/3}\text{Co}_{1/3}\text{Mn}_{1/3}\text{O}_2$, and LiMn_2O_4 in Bulk All-Solid-State Batteries. *Chem. Mater.* **2017**, 29 (9), 3883–3890.
- (2) Auvergniot, J.; Cassel, A.; Foix, D.; Viallet, V.; Seznec, V.; Dedryvère, R. Redox activity of argyrodite Li₆PS₅Cl electrolyte in all-solid-state Li-ion battery: An XPS study. *Solid State Ionics* **2017**, 300, 78–85
- (3) Homma, K.; Yonemura, M.; Kobayashi, T.; Nagao, M.; Hirayama, M.; Kanno, R. Crystal structure and phase transitions of the lithium ionic conductor Li₃PS₄. *Solid State Ionics* **2011**, *182* (1), 53–58.
- (4) Murayama, M.; Sonoyama, N.; Yamada, A.; Kanno, R. Material design of new lithium ionic conductor, thio-LISICON, in the $\text{Li}_2\text{S}-\text{P}_2\text{S}_5$ system. *Solid State Ionics* **2004**, *170* (3), 173–180.
- (5) de Klerk, N. J. J.; Rosłoń, I.; Wagemaker, M. Diffusion Mechanism of Li Argyrodite Solid Electrolytes for Li-Ion Batteries and Prediction of Optimized Halogen Doping: The Effect of Li Vacancies, Halogens, and Halogen Disorder. *Chem. Mater.* **2016**, 28 (21), 7955–7963.
- (6) Sedlmaier, S. J.; Indris, S.; Dietrich, C.; Yavuz, M.; Dräger, C.; von Seggern, F.; Sommer, H.; Janek, J. Li₄PS₄I: A Li⁺ Superionic Conductor Synthesized by a Solvent-Based Soft Chemistry Approach. *Chem. Mater.* **2017**, *29* (4), 1830–1835.
- (7) Liu, X.; Chen, Y.; Hood, Z. D.; Ma, C.; Yu, S.; Sharafi, A.; Wang, H.; An, K.; Sakamoto, J.; Siegel, D. J.; Cheng, Y.; Jalarvo, N. H.; Chi, M., Elucidating the mobility of H⁺ and Li⁺ ions in (Li_{6.25-x}H_xAl_{0.25})-La₃Zr₂O₁₂ via correlative neutron and electron spectroscopy. *Energy Environ. Sci.* **2019**, *12*, 945–951.
- (8) Hood, Z. D.; Wang, H.; Samuthira Pandian, A.; Keum, J. K.; Liang, C. Li₂OHCl Crystalline Electrolyte for Stable Metallic Lithium Anodes. *J. Am. Chem. Soc.* **2016**, *138* (6), 1768–1771.
- (9) Deng, Y.; Eames, C.; Nguyen, L. H. B.; Pecher, O.; Griffith, K. J.; Courty, M.; Fleutot, B.; Chotard, J.-N.; Grey, C. P.; Islam, M. S.; Masquelier, C. Crystal Structures, Local Atomic Environments, and Ion Diffusion Mechanisms of Scandium-Substituted Sodium Superionic Conductor (NASICON) Solid Electrolytes. *Chem. Mater.* **2018**, 30 (8), 2618–2630.

(10) Suzuki, N.; Richards, W. D.; Wang, Y.; Miara, L. J.; Kim, J. C.; Jung, I.-S.; Tsujimura, T.; Ceder, G. Synthesis and Electrochemical Properties of I4-Type Li_{1+2x}Zn_{1-x}PS₄ Solid Electrolyte. *Chem. Mater.* **2018**, 30 (7), 2236–2244.

- (11) Kaup, K.; Lalère, F.; Huq, A.; Shyamsunder, A.; Adermann, T.; Hartmann, P.; Nazar, L. F. Correlation of Structure and Fast Ion Conductivity in the Solid Solution Series Li_{1 + 2x}Zn_{1-x}PS₄. *Chem. Mater.* **2018**, 30 (3), 592–596.
- (12) Aihara, Y.; Ito, S.; Omoda, R.; Yamada, T.; Fujiki, S.; Watanabe, T.; Park, Y.; Doo, S., The Electrochemical Characteristics and Applicability of an Amorphous Sulfide-Based Solid Ion Conductor for the Next-Generation Solid-State Lithium Secondary Batteries. *Front. Energy Res.* **2016**, *4* (18). DOI: 10.3389/fenrg.2016.00018
- (13) Miara, L.; Windmüller, A.; Tsai, C.-L.; Richards, W. D.; Ma, Q.; Uhlenbruck, S.; Guillon, O.; Ceder, G. About the Compatibility between High Voltage Spinel Cathode Materials and Solid Oxide Electrolytes as a Function of Temperature. *ACS Appl. Mater. Interfaces* **2016**, *8* (40), 26842–26850.
- (14) Uhlenbruck, S.; Dornseiffer, J.; Lobe, S.; Dellen, C.; Tsai, C.-L.; Gotzen, B.; Sebold, D.; Finsterbusch, M.; Guillon, O. Cathode-electrolyte material interactions during manufacturing of inorganic solid-state lithium batteries. *J. Electroceram.* **2017**, 38 (2), 197–206.
- (15) Hayashi, A.; Sakuda, A.; Tatsumisago, M., Development of Sulfide Solid Electrolytes and Interface Formation Processes for Bulk-Type All-Solid-State Li and Na Batteries. *Front. Energy Res.* **2016**, 4 (25). DOI: 10.3389/fenrg.2016.00025
- (16) Knauth, P. Inorganic solid Li ion conductors: An overview. *Solid State Ionics* **2009**, *180* (14), 911–916.
- (17) Park, K. H.; Bai, Q.; Kim, D. H.; Oh, D. Y.; Zhu, Y.; Mo, Y.; Jung, Y. S. Design Strategies, Practical Considerations, and New Solution Processes of Sulfide Solid Electrolytes for All-Solid-State Batteries. Advanced Energy Materials 2018, 8 (18), 1800035.
- (18) Xiong, S.; Liu, Z.; Rong, H.; Wang, H.; McDaniel, M.; Chen, H. Na₃SbSe_{4-x}S_x as Sodium Superionic Conductors. *Sci. Rep.* **2018**, 8 (1), 9146.
- (19) Kanno, R.; Murayama, M. Lithium Ionic Conductor Thio-LISICON: The Li₂S-GeS₂-P₂S₅ System. *J. Electrochem. Soc.* **2001**, *148* (7), A742–A746.
- (20) Yu, C.; Ganapathy, S.; van Eck, E. R. H.; van Eijck, L.; Basak, S.; Liu, Y.; Zhang, L.; Zandbergen, H.; Wagemaker, M. Revealing the relation between the structure, Li-ion conductivity and solid-state battery performance of the argyrodite Li₆PS₅Br solid electrolyte. *J. Mater. Chem. A* **2017**, *5*, 21178.
- (21) Deiseroth, H.-J.; Maier, J.; Weichert, K.; Nickel, V.; Kong, S.-T.; Reiner, C. Li₇PS₆ and Li₆PS₅X (X: Cl, Br, I): Possible Three-dimensional Diffusion Pathways for Lithium Ions and Temperature Dependence of the Ionic Conductivity by Impedance Measurements. *Z. Anorg. Allg. Chem.* **2011**, *637* (10), 1287–1294.
- (22) Rao, R. P.; Adams, S. Studies of lithium argyrodite solid electrolytes for all-solid-state batteries. *Phys. Status Solidi A* **2011**, 208 (8), 1804–1807.
- (23) Ziolkowska, D. A.; Arnold, W.; Druffel, T.; Sunkara, M.; Wang, H. Rapid and Economic Synthesis of a Li₇PS₆ Solid Electrolyte from a Liquid Approach. *ACS Appl. Mater. Interfaces* **2019**, *11* (6), 6015–6021.
- (24) Yamane, H.; Shibata, M.; Shimane, Y.; Junke, T.; Seino, Y.; Adams, S.; Minami, K.; Hayashi, A.; Tatsumisago, M. Crystal structure of a superionic conductor, $\text{Li}_7\text{P}_3\text{S}_{11}$. *Solid State Ionics* **2007**, *178* (15), 1163–1167.
- (25) Kamaya, N.; Homma, K.; Yamakawa, Y.; Hirayama, M.; Kanno, R.; Yonemura, M.; Kamiyama, T.; Kato, Y.; Hama, S.; Kawamoto, K.; Mitsui, A. A lithium superionic conductor. *Nat. Mater.* **2011**, *10* (9), 682–686.
- (26) Brant, J. A.; Massi, D. M.; Holzwarth, N. A. W.; MacNeil, J. H.; Douvalis, A. P.; Bakas, T.; Martin, S. W.; Gross, M. D.; Aitken, J. A. Fast Lithium Ion Conduction in Li₂SnS₃: Synthesis, Physicochemical Characterization, and Electronic Structure. *Chem. Mater.* **2015**, 27 (1), 189–196.

- (27) Kraft, M. A.; Culver, S. P.; Calderon, M.; Böcher, F.; Krauskopf, T.; Senyshyn, A.; Dietrich, C.; Zevalkink, A.; Janek, J.; Zeier, W. G. Influence of Lattice Polarizability on the Ionic Conductivity in the Lithium Superionic Argyrodites Li_6PS_5X (X = Cl, Br, I). *J. Am. Chem. Soc.* **2017**, *139* (31), 10909–10918.
- (28) Kraft, M. A.; Ohno, S.; Zinkevich, T.; Koerver, R.; Culver, S. P.; Fuchs, T.; Senyshyn, A.; Indris, S.; Morgan, B. J.; Zeier, W. G. Inducing High Ionic Conductivity in the Lithium Superionic Argyrodites $\text{Li}_{6+x}\text{P}_{1-x}\text{Ge}_x\text{S}_5\text{I}$ for All-Solid-State Batteries. *J. Am. Chem. Soc.* **2018**, *140* (47), 16330–16339.
- (29) Zhu, Z.; Chu, I.-H.; Ong, S. P. Li $_3$ Y(PS $_4$) $_2$ and Li $_5$ PS $_4$ Cl $_2$: New Lithium Superionic Conductors Predicted from Silver Thiophosphates using Efficiently Tiered Ab Initio Molecular Dynamics Simulations. *Chem. Mater.* **2017**, 29 (6), 2474–2484.
- (30) Haomin, C. Computational design of inorganic ionic conductors. Thesis, National University of Singapore, Scholar-Bank@NUS Repository, 2017.
- (31) Toby, B. H.; Von Dreele, R. B. GSAS-II: the genesis of a modern open-source all purpose crystallography software package. *J. Appl. Crystallogr.* **2013**, *46* (2), 544–549.
- (32) Perl, J.; Shin, J.; Schümann, J.; Faddegon, B.; Paganetti, H. TOPAS: An innovative proton Monte Carlo platform for research and clinical applications. *Med. Phys.* **2012**, *39* (11), 6818–6837.
- (33) Juhas, P.; Davis, T.; Farrow, C. L.; Billinge, S. J. L. PDFgetX3: a rapid and highly automatable program for processing powder diffraction data into total scattering pair distribution functions. *J. Appl. Crystallogr.* **2013**, *46* (2), 560–566.
- (34) Farrow, C. L.; Juhas, P.; Liu, J. W.; Bryndin, D.; Božin, E. S.; Bloch, J.; Proffen, Th.; Billinge, S. J. L. PDFfit2 and PDFgui: computer programs for studying nanostructure in crystals. *J. Phys.: Condens. Matter* **2007**, *19* (33), 335219.
- (35) Duer, M. J. Introduction to Solid-State NMR Spectroscopy; Blackwell Publishing: Oxford, U.K., 2004.
- (36) Fukushima, E.; Roeder, S. B. W. Experimental Pulse NMR—A Nuts and Bolts Approach; Addison-Wesley: Reading, PA, 1981.
- (37) Heitjans, P.; Indris, S.; Wilkening, M. Solid-State Diffusion and NMR. *Diffus. Fundam.* **2005**, 2 (45), 1–20.
- (38) Price, W. S. Pulsed-field gradient nuclear magnetic resonance as a tool for studying translational diffusion: Part 1. Basic theory. *Concepts Magn. Reson.* **1997**, *9* (5), 299–336.
- (39) Kresse, G.; Furthmuller, J. Efficient iterative schemes for ab initio total-energy calculations using a plane-wave basis set. *Phys. Rev. B: Condens. Matter Mater. Phys.* **1996**, 54 (16), 11169–11186.
- (40) Perdew, J. P.; Ernzerhof, M.; Burke, K. Rationale for mixing exact exchange with density functional approximations. *J. Chem. Phys.* **1996**, *105* (22), 9982–9985.
- (41) Nose, S. Constant temperature molecular dynamics methods. *Prog. Theor. Phys. Suppl.* **1991**, *103*, 1–46.
- (42) He, X.; Zhu, Y.; Epstein, A.; Mo, Y. Statistical variances of diffusional properties from ab initio molecular dynamics simulations. *Npj Computational Materials* **2018**, *4* (1), 18.
- (43) Wang, Y.; Lu, D.; Bowden, M.; El Khoury, P. Z.; Han, K. S.; Deng, Z. D.; Xiao, J.; Zhang, J.-G.; Liu, J. Mechanism of Formation of Li7P3S11 Solid Electrolytes through Liquid Phase Synthesis. *Chem. Mater.* **2018**, 30 (3), 990–997.
- (44) Holzwarth, N. A. W.; Lepley, N. D.; Du, Y. A. Computer modeling of lithium phosphate and thiophosphate electrolyte materials. *J. Power Sources* **2011**, *196* (16), 6870–6876.
- (45) Deng, Z.; Zhu, Z.; Chu, I.-H.; Ong, S. P. Data-Driven First-Principles Methods for the Study and Design of Alkali Superionic Conductors. *Chem. Mater.* **2017**, 29 (1), 281–288.
- (46) Dietrich, C.; Weber, D. A.; Culver, S.; Senyshyn, A.; Sedlmaier, S. J.; Indris, S.; Janek, J.; Zeier, W. G. Synthesis, Structural Characterization, and Lithium Ion Conductivity of the Lithium Thiophosphate $\text{Li}_2P_2S_6$. Inorg. Chem. **2017**, 56 (11), 6681–6687.
- (47) Dietrich, C.; Sadowski, M.; Sicolo, S.; Weber, D. A.; Sedlmaier, S. J.; Weldert, K. S.; Indris, S.; Albe, K.; Janek, J.; Zeier, W. G. Local Structural Investigations, Defect Formation, and Ionic Conductivity of

the Lithium Ionic Conductor Li4P2S6. Chem. Mater. 2016, 28 (23), 8764-8773.

- (48) Jörgens, S.; Mewis, A. $Ag_5PS_4Cl_2$ and $Ag_{15}(PS_4)_4Cl_3$ Crystal structures and their relation to Ag3PS4. *Solid State Sci.* **2007**, 9 (2), 213–217.
- (49) Shannon, R. Revised effective ionic radii and systematic studies of interatomic distances in halides and chalcogenides. *Acta Crystallogr., Sect. A: Cryst. Phys., Diffr., Theor. Gen. Crystallogr.* **1976**, 32 (5), 751–767.
- (50) Seino, Y.; Ota, T.; Takada, K.; Hayashi, A.; Tatsumisago, M. A sulphide lithium super ion conductor is superior to liquid ion conductors for use in rechargeable batteries. *Energy Environ. Sci.* **2014**, 7 (2), 627–631.
- (51) Vinod Chandran, C.; Pristat, S.; Witt, E.; Tietz, F.; Heitjans, P. Solid-State NMR Investigations on the Structure and Dynamics of the Ionic Conductor $\text{Li}_{1+x}\text{Al}_x\text{Ti}_{2-x}(\text{PO}_4)_3$ (0.0 $\leq x \leq$ 1.0). *J. Phys. Chem.* C **2016**, 120 (16), 8436–8442.
- (52) Wilkening, M.; Heitjans, P. Li jump process in h-Li_{0.7}TiS₂ studied by two-time ⁷Li spin-alignment echo NMR and comparison with results on two-dimensional diffusion from nuclear magnetic relaxation. *Phys. Rev. B: Condens. Matter Mater. Phys.* **2008**, 77 (2), 024311
- (53) Stejskal, E. O.; Tanner, J. E. Spin Diffusion Measurements: Spin Echoes in the Presence of a Time-Dependent Field Gradient. *J. Chem. Phys.* **1965**, 42 (1), 288–292.